Active control of the acoustic boundary conditions of combustion test rigs

Mirko R. Bothien*, Jonas P. Moeck, Christian Oliver Paschereit

Institut für Strömungsmechanik und Technische Akustik, Technische Universität Berlin, 10623 Berlin, Germany

Abstract

In the design process of burners for gas turbines, new burner generations are generally tested in single or multi burner combustion test rigs. With these experiments, computational fluid dynamics, and finite element calculations, the burners' performance in the full-scale engine is sought to be predicted. Especially, information about the thermoacoustic behaviour and the emission characteristics is very important. As the thermoacoustics strongly depend on the acoustic boundary conditions of the system, it is obvious that test rig conditions should match, or be close to those of the full-scale engine. This is, however, generally not the case. Hence, if the combustion process in the test rig is stable at certain operating conditions, it may show unfavourable dynamics at the same conditions in the engine. In this work, a method is proposed which uses an active control scheme to manipulate the acoustic boundary conditions of the test rig. Using this method, the boundary conditions can be continuously modified, ranging from anechoic to fully reflecting in a broad frequency range. The concept is applied to an atmospheric combustion test rig with a swirl-stabilized burner. It is shown that the test rig's properties can be tuned to correspond to those of the full-scale engine. For example, the test rig length can be virtually extended, thereby introducing different resonance frequencies, without having to implement any hardware changes. Furthermore, the acoustic boundary condition can be changed to that of a choked flow without actually needing the flow to be choked.

1. Introduction

One of the main issues in gas turbine development is the stability of the combustion process. In order to follow stringent NO_x emission restrictions, lean-premixed combustion was introduced by the gas turbine industry. Combustion systems operating in this mode are, however, susceptible to self-excited oscillations arising due to the interaction of the unsteady heat release and the acoustic field in the combustion chamber. If the two mechanisms constructively interfere, high amplitude pressure and heat release fluctuations occur, which have a detrimental effect on the combustion process. These so-called thermoacoustic instabilities cause

*Corresponding author. Tel.: +49 30 314 23111; fax.: +49 30 314 21101.

E-mail address: mirko.bothien@tu-berlin.de (M.R. Bothien).

Nomenclature

c	speed of sound	x	axial coordinate
D	wave decomposer	Z	(specific) acoustic impedance
e	control command		
f	frequency	λ	wave-length
f	downstream travelling wave	ρ	density
g	upstream travelling wave	τ	time-delay
G	loudspeaker transfer function	φ	phase angle
i	imaginary unit	ϕ	equivalence ratio
j	integer	ω	angular frequency
k	wave number		
K	controller transfer function	*Subscripts and superscripts*	
l	length		
M	Mach number	cl	closed-loop
n	integer	ol	open-loop
p	acoustic pressure scaled by ρc	ref	reference
q	fluctuation of OH-radical	us	upstream
R	reflection coefficient	$(\cdot)^-$	against mean flow direction
t	time	$(\cdot)^+$	in mean flow direction
U_0	mean flow velocity	$(\cdot)^+$	pseudo inverse
v	axial acoustic particle velocity	$\hat{(\cdot)}$	Fourier transform

structural wear, increase noise and pollutant emissions, and can even lead to engine failure [1,2]. Therefore, designing burners which promote a stable combustion process is an important task.

Assessing the quality of new burner concepts in the design phase is usually accomplished by means of extensive experimental investigations at combustor test rigs [3,4]. These experiments in conjunction with computational fluid dynamics (CFD) and finite element calculations are then used to predict the burner's performance in the full-scale engine. The quality of this prediction, however, can only be verified at the very end of the design process after the burner is tested in the full-scale engine. At this point, changes in component design are very expensive and will cause severe delays in the schedule [3]. This underlines the need for a procedure allowing a reliable prediction of burner behaviour in the engine. Alternatives to component design modifications then are only active and passive means to mitigate thermoacoustic instabilities. Numerous research groups have been working on these topics. However, only a few publications exist reporting the implementation of these concepts in the real engine. Engine applications of active control strategies were shown by Seume et al. [5] and Richards et al. [6]. Passive means are more common and were, for example, presented by Bellucci et al. [7] and Berenbrink and Hoffmann [8]. More information and references for engine applications were summarized in a comprehensive review on passive control strategies in gas turbines conducted by Richards et al. [9]. Different industrial approaches can also be found in Ref. [1].

Generally, the acoustic characteristics of the test rig are significantly different from those of the full-scale engine, thus, complicating the prediction. This is due to the fact that not only the static pressures and temperatures are higher, but also the geometries are different [10]. Thermoacoustic instabilities usually appear close to the acoustic resonance frequencies of the combustion chamber, whenever the flame response at these frequencies is sufficiently large and the phase relationships involved promote constructive interference [1,11]. For this reason, a burner that shows a desirable behaviour with respect to pressure pulsations and emissions in the test rig might exhibit essentially different characteristics in the engine. This is due to the fact that the thermoacoustics of the engine are properly represented by the test rig only if both, the dynamic flame response (significantly influenced by the burner) and the acoustic boundary conditions, match.

Accounting for different acoustic boundary conditions by means of design modifications of the test rig is expensive and time-consuming. Mongia et al. [3] presented a laboratory scale combustor whose resonance frequencies could conveniently be changed. The test rig basically consisted of an upstream tube, the burner, and a downstream tube. The tubes' lengths could be continuously varied using perforated pistons. Through this, the test rig's resonances could be continuously varied. The combustion group at Georgia Tech uses a similar setup to be able to tune the upstream end of their combustion test facility [12]. Although in both cases a change of test rig resonances is quite straightforward, the degree of reflectivity remained constant and problems are to be expected when applying the system to industrial test rigs with higher power, i.e., higher mass flows and elevated pressures. Another way to adjust the boundary conditions to those of the engine is followed here by actively tuning (i.e., artificially changing) them. This can be done by using an active control scheme, which detects the acoustic field at the combustion chamber outlet and feeds back a suitable signal to drive an acoustic actuator. The actuator modifies the acoustic field in the system to match the desired one. An additional advantage of this method is that the same test rig can be used to simulate the acoustic conditions of different full-scale engines. Also, by incorporating the real acoustic boundary conditions to the test rig, it is possible to have a realistic estimate about the whole combustion process subject to the engine acoustics, like, e.g., NO_x emissions.

The underlying idea is that the impact of a geometry change on the plane wave acoustic field *physically* can be represented by a change of the impedance at a certain position. In the following, the setup depicted in Fig. 1 is considered. The system is connected to a duct, in which only plane waves propagate, terminated with an acoustic boundary condition Z_1. Here, Z denotes the acoustic impedance, a complex valued function of frequency. The acoustic impedance is defined as

$$Z = \frac{\hat{p}}{\hat{v}}, \tag{1}$$

where $\hat{p}$ and $\hat{v}$ denote Fourier transforms of acoustic pressure and particle velocity normal to the boundary, respectively. Here, as in the following, the acoustic pressure has been scaled by the characteristic impedance ρc, ρ being the fluid density and c the speed of sound.

The system considered in Fig. 1 has certain characteristics depending on the acoustic field associated with Z_1. For other acoustic boundary conditions, e.g., induced by a change in geometry (Z_2) or by some damping device mounted in the duct (Z_3), the system may exhibit essentially different characteristics. This can be due to higher or lower resonance frequencies or increased damping, for example. The aim of the control scheme to be presented is to mimic certain prescribed impedances. In this way, the impact of different acoustic boundary conditions on the system characteristics can be studied, without actually implementing the devices that alter the boundary impedance.

Guicking and Karcher [13] introduced the concept of changing the impedance through active control of the acoustic boundary condition in 1984. They were able to realize reflection coefficients ranging from fully absorbing to fully reflecting. However, they only considered fixed frequency harmonic signals and tuned the control parameters empirically. Furthermore, only a system without mean flow and combustion was considered. Furstoss et al. [14] and Smith et al. [15] actively changed the impedance to increase the sound absorption of porous layers. Their approaches, however, only aimed to produce anechoic terminations and the sensor/controller setups are confined to specific applications and not suited for combustion experiments. Application of this concept was also presented in Ref. [16], where a similar method was used to reduce the resonator length of a thermoacoustic cooler.
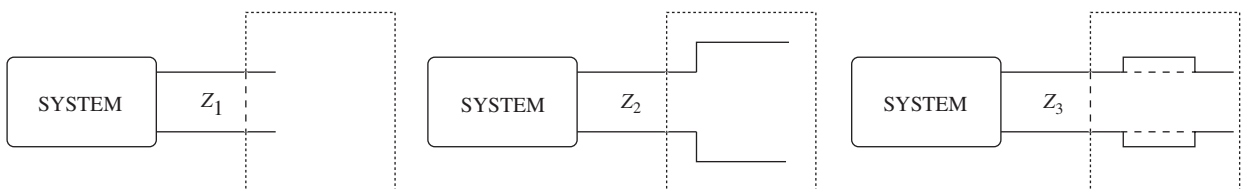

Fig. 1. System with different acoustic boundary conditions induced by a change in geometry or by implementation of a liner.

Another application of the impedance tuning concept lies in the stability analysis of gas turbine combustors. Here, the common approach is to predict stability properties by setting up so-called network models [17–20]. In this approach, the dynamic features of the flame response, represented by the flame transfer function/matrix, are coupled to a low-order model of the combustion chamber acoustics. Low-order acoustic models are sufficiently mature to accurately capture complex engine geometries either analytically or by using finite element computations [21,22]. The flame transfer function of industrial burners involves the most complex mechanisms—interaction between flow, acoustics, and combustion—and therefore can only be reliably obtained from experiments in test rigs. Recently, there has been some effort to determine flame transfer functions by using CFD computations [23,24]. However, the most accurate and reliable method still seems to be the experiment.

Instead of integrating the dynamic flame properties, as obtained from test rig measurements, into models of the engine geometry, the impedance tuning approach could be used to transfer the engine geometry to the test rig by means of its acoustic characteristics. Hence, this is an alternative way to assess thermoacoustic stability of a burner subject to machine acoustics.

Bothien et al. [25] used the concept of active boundary control to validate linear stability analyses with experimental data. By tuning the downstream reflectivity of a combustion test rig, the predictive capabilities of a network model regarding frequency of instability, linear growth rate, and transition from stability to instability could be assessed.

2. Control approach

2.1. Control principle

To develop the control scheme, the setup in Fig. 2 is considered. The duct whose end-impedance is to be manipulated is equipped with a sensor array, consisting of several microphones at different axial positions and an actuator. To achieve the control objective, the sensor signals are fed to a control scheme, which generates the command signal and acts on the acoustic field via the actuator. It is more convenient to consider the downstream propagating wave f as the actual control input. For this reason, the control scheme depicted in Fig. 2 has been split into two parts: (i) a wave decomposer, labelled D, that extracts the downstream propagating wave from the pressure signals p_j; and (ii) the actual control law K. Accordingly, finding a wave decomposition scheme D that works accurately over a range of frequencies is necessary. A method for time domain wave separation is presented in Section 3. For the remainder of this part, the f-wave is considered to be known so that it can serve as the input to the controller.

The problem now is to find a suitable K that, given the downstream propagating wave f, is able to drive the actuator in such a way that the closed-loop reflection coefficient R_{cl} is close to the desired one. The control law K can be built if the uncontrolled (or open-loop) reflection coefficient R_{ol} and the actuator transfer function are known, as will be shown below. In contrast to Guicking and Karcher's approach [13], there is no need for manual parameter tuning and the controller acts over a range of frequencies. Also, the scheme presented here
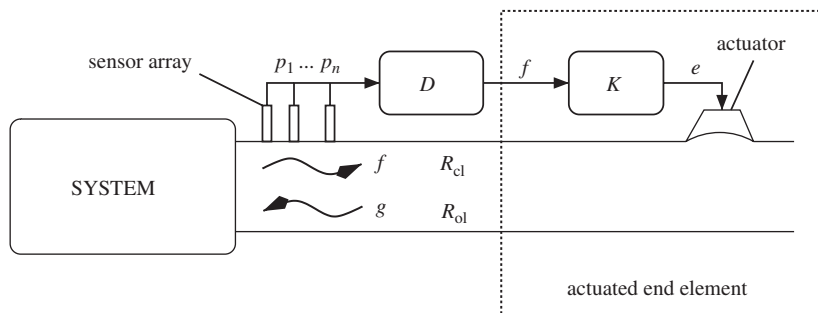

Fig. 2. System with controlled acoustic boundary conditions. The wave decomposer D extracts the downstream propagating wave f from multiple pressure measurements p_j. Based on f, the controller K generates the actuation command e. The uncontrolled reflection coefficient R_{ol} is manipulated by the control scheme and the actuator so that the system is exposed to a reflection coefficient given by R_{cl}.

will not only work for time-harmonic but also for transient signals. This is particularly important when considering combustion noise, where no distinct frequencies prevail.

2.2. Control law

In this study, only plane wave acoustic fields are considered, where the acoustic pressure and the axial particle velocity only depend on the axial coordinate. Practically, this means that only frequencies below the cut-on frequency for the first non-planar mode can be accounted for. For the control approach considered here, a more convenient notation makes use of the Riemann invariants f and g, which can be thought of as the down- and upstream travelling waves. They are related to the primitive acoustic variables by

$$p = f + g, \tag{2a}$$

$$v = f - g. \tag{2b}$$

Due to linearity, Eqs. (2) hold in frequency as well as in time domain.

In Section 1, the acoustic boundary condition was expressed as the impedance Z, the ratio of acoustic pressure and particle velocity, $Z = \hat{p}/\hat{v}$. Equivalently, the reflection coefficient R is defined as the ratio of the reflected to the incident wave, $R = \hat{g}/\hat{f}$. Using Eqs. (2), it is found that the reflection coefficient is related to the impedance by

$$R = \frac{Z - 1}{Z + 1}. \tag{3}$$

To derive a suitable control law, a model for the actuated end element (Fig. 2) is written as

$$\hat{g} = R_{\mathrm{ol}}\hat{f} + G\hat{e}, \tag{4}$$

where G is the actuator transfer function and $\hat{e}$ is the control command. R_{ol} and G can both be obtained experimentally from frequency response measurements in conjunction with the multi-microphone method (MMM [18,26,27], see also Sections 2.3 and 3). In Eq. (4), it is assumed that the outgoing $\hat{g}$-wave can be obtained as a linear superposition of the geometrical reflection of the incident wave $\hat{f}$ and the wave generation due to the actuator. Validity of this assumption was previously shown in Ref. [18].

Given that $\hat{f}$ can be extracted from the microphone signals and is fed to the controller ($\hat{e} = K\hat{f}$), the end element's $\hat{g}$ response reads

$$\hat{g} = (R_{\mathrm{ol}} + GK)\hat{f}. \tag{5}$$

Hence, the closed-loop reflection coefficient is given by

$$R_{\mathrm{cl}} = \frac{\hat{g}}{\hat{f}} = R_{\mathrm{ol}} + GK. \tag{6}$$

If the uncontrolled reflection coefficient R_{ol} and the actuator transfer function G are known, then, given a desired reflection coefficient R_{cl}, the control law K can be calculated from

$$K = \frac{R_{\mathrm{cl}} - R_{\mathrm{ol}}}{G}. \tag{7}$$

It remains to specify a scheme which is able to extract the incident wave from multiple simultaneous pressure measurements online, i.e., in time domain. Such a scheme will be presented in Section 3.

2.3. Model identification

The controller transfer function K has to be computed according to Eq. (7). In essence, this means to identify the model for the $\hat{g}$ response of the actuated end element given by Eq. (4). The uncontrolled reflection coefficient and the actuator transfer function can be identified using the MMM and two independent excitation states. Excitation with the upstream woofer and application of the MMM yields the uncontrolled reflection coefficient R_{ol}, as $\hat{e} = 0$ in Eq. (4). Subsequent excitation with the downstream speaker and further

application of the MMM allows to compute the speaker transfer function G from Eq. (4)

$$G = \frac{\hat{g} - R_{ol}\hat{f}}{\hat{e}},$$

(8)

taking into account the reflection coefficient R_{ol} calculated in the previous step.

The basis for determining the experimental frequency response is the decomposition of the plane wave acoustic field into its up- and downstream propagating parts $\hat{g}$ and $\hat{f}$. Simply using the frequency domain representations of Eqs. (2) is not possible since the acoustic velocity cannot be measured directly with sufficient accuracy. However, since the analytic form of the plane acoustic field is known, multiple axially distributed pressure measurements can be used to find a good approximation to the Riemann invariants in frequency domain.

In a duct of constant cross-section with negligible visco-thermal dissipation, the plane wave acoustic field can be written as [28]

$$\hat{p}(x,\omega) = \hat{f}(\omega)e^{-ik^+x} + \hat{g}(\omega)e^{ik^-x},$$

(9a)

$$\hat{v}(x,\omega) = \hat{f}(\omega)e^{-ik^+x} - \hat{g}(\omega)e^{ik^-x},$$

(9b)

where $k^\pm = \omega/(c \pm U_0)$ are the propagation constants. Here, ω is the angular frequency, c the speed of sound, and U_0 the mean flow velocity. Given the experimentally determined pressure phasors $\hat{p}$ at multiple axial locations, Eqs. (9) can be formally inverted in a least squares sense to yield

$$\begin{bmatrix} \hat{f}(\omega) \\ \hat{g}(\omega) \end{bmatrix} = \mathbf{H}^+ \begin{bmatrix} \hat{p}(x_1,\omega) \\ \hat{p}(x_2,\omega) \\ \vdots \\ \hat{p}(x_n,\omega) \end{bmatrix},$$

(10)

where $\mathbf{H}$ is given by

$$\mathbf{H} = \begin{bmatrix} e^{-ik^+x_1} & e^{ik^-x_1} \\ e^{-ik^+x_2} & e^{ik^-x_2} \\ \vdots & \vdots \\ e^{-ik^+x_n} & e^{ik^-x_n} \end{bmatrix},$$

(11)

and $(\cdot)^+$ denotes the pseudoinverse of a matrix. In this way, $\hat{f}$ and $\hat{g}$ are obtained from the pressure phasors and can be used to calculate R_{ol} and G.

The procedure explained above provides the controller transfer function K as discrete frequency response data. However, to apply it in a control scheme, a model accurately capturing the response is necessary. In this study, the models were obtained by using frequency domain system identification algorithms [29].

3. Schemes for online wave decomposition

As the f-wave is the control input, a suitable algorithm is required that separates the up- and downstream travelling waves from the pressure sensor signals. In frequency domain, this can be accomplished by using the well-known MMM [18,26,27]. However, in contrast to the works cited, here, the wave decomposition cannot be performed as a post-processing step. The f-wave has to be identified *online* and its calculation from the sound pressure sensors has to be accomplished in time domain. This can be done by first noting that the Riemann invariants in a uniform duct are only functions of retarded arguments,

$$f = f(t - x/(c + U_0)),$$
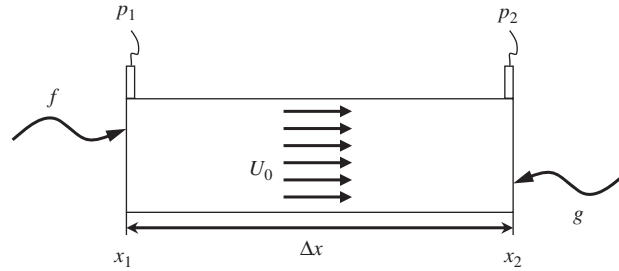
(12a)

$$g = g(t + x/(c - U_0)).$$

(12b)

Fig. 3. Setup for online wave identification with two microphones.
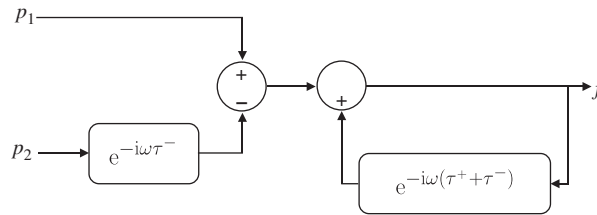

Fig. 4. Block diagram mapping two measured pressures to the downstream travelling wave f.

With reference to Fig. 3, Eqs. (12) are evaluated at two axial locations, x_1 and x_2 (say), to give the relations

$$p_1(t) = f(t) + g(t - \tau^-), \tag{13}$$

$$p_2(t) = f(t - \tau^+) + g(t), \tag{14}$$

where $\tau^{\pm} = \Delta x/(c \pm U_0)$ and $\Delta x = x_2 - x_1$. In these equations, g can be eliminated by evaluating Eq. (14) at $t - \tau^-$ and using the result in Eq. (13) to yield

$$p_1(t) = f(t) + p_2(t - \tau^-) - f(t - \tau^- - \tau^+), \tag{15}$$

from which it is concluded that the f-wave can be identified in real-time by using the scheme shown in Fig. 4.

One drawback of this approach is that the feedback loop in Fig. 4 is only marginally stable. To see this, Eq. (15) is solved for $\hat{f}$ in frequency domain:

$$\hat{f} = \frac{\hat{p}_1 - \hat{p}_2 e^{-i\omega\tau^-}}{1 - e^{-i\omega(\tau^+ + \tau^-)}}. \tag{16}$$

The purely real eigenvalues are located at

$$\omega_n = \frac{2\pi n}{\tau^+ + \tau^-}, \quad n = 0, \pm 1, \pm 2 \ldots . \tag{17}$$

This relation can be recast in the form

$$\frac{\omega_n}{c}\Delta x = \pi n(1 - M^2), \tag{18}$$

where M is the Mach number. This equation was given by Åbom and Bodén [30] in the analysis of the two-microphone-method (TMM) in frequency domain. For small Mach numbers, Eq. (17) is satisfied when the microphone spacing matches half the wave-length. It is important to note that, as the above authors pointed out, not only are the frequencies given in Eq. (17) excluded from data processing, but the error in the TMM increases dramatically close to these frequencies. Also, decreasing the microphone spacing to move ω_1 to higher frequencies is not an option since, in this case, the accuracy of the TMM significantly deteriorates at low frequencies [30].

In practice, this means that the identification algorithm cannot be used close to frequencies for which Eq. (17) holds. Moreover, oscillations can be excited that would have to be suppressed with suitable notch filters. In the frequency domain, this issue is resolved by using the MMM. Here, several microphones at different axial locations, corresponding to unequal propagation delays, are used. This resolves the issue of singularities at frequencies given by Eq. (17). The wave decomposition is then obtained from a least squares fit to the measured complex pressure amplitudes. Another advantage of the MMM is that, by averaging over several microphones, flow noise is suppressed. This is even more important in a real-time application, where noise rejection techniques, such as cross-correlations with the excitation signal, cannot be used. The traditional MMM is applied in a post-processing step, where pressure records for a certain time interval are available. For the impedance tuning control scheme, the decomposition has to be accomplished in real-time. Therefore, application of the traditional MMM is not straightforward. However, a time domain scheme, having similar advantages like the MMM in frequency domain (i.e., using more pressure signals to reject flow noise and removal of singular frequencies), can be constructed as follows. With respect to the setup shown in Fig. 5, n equations for the pressure signals are obtained as

$$p_1(t) = f(t) + g(t), \tag{19a}$$

$$p_2(t) = f(t - \tau_{1,2}^+) + g(t + \tau_{1,2}^-), \tag{19a}$$

$$\vdots$$

$$p_n(t) = f(t - \tau_{1,n}^+) + g(t + \tau_{1,n}^-), \tag{19a}$$

where $\tau_{n,m}^{\pm} = (x_m - x_n)/(c \pm U_0)$. The aim is now to find a causal relation for $f(t)$ that accounts for all n pressure recordings. The pressure at location x_k is written at time $t - \tau_{1,k}^-$, viz.,

$$p_1(t) = f(t) + g(t), \tag{20a}$$

$$p_2(t - \tau_{1,2}^-) = f(t - \tau_{1,2}^+ - \tau_{1,2}^-) + g(t), \tag{20a}$$

$$\vdots$$

$$p_n(t - \tau_{1,n}^-) = f(t - \tau_{1,n}^+ - \tau_{1,n}^-) + g(t). \tag{20a}$$

Eqs. (20) are now considered as an overdetermined linear system for $f(t)$ and $g(t)$, whose least squares solution takes the form

$$\begin{bmatrix} f(t) \\ g(t) \end{bmatrix} = \begin{bmatrix} 1 & -1/(n-1) & \dots & -1/(n-1) \\ 0 & 1/(n-1) & \dots & 1/(n-1) \end{bmatrix} \begin{bmatrix} p_1(t) \\ p_2(t - \tau_{1,2}^-) - f(t - \tau_{1,2}^+ - \tau_{1,2}^-) \\ \vdots \\ p_n(t - \tau_{1,n}^-) - f(t - \tau_{1,n}^+ - \tau_{1,n}^-) \end{bmatrix}. \tag{21}$$
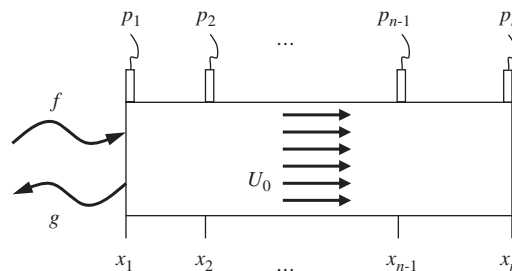

Fig. 5. Setup for online wave identification with multiple microphones.
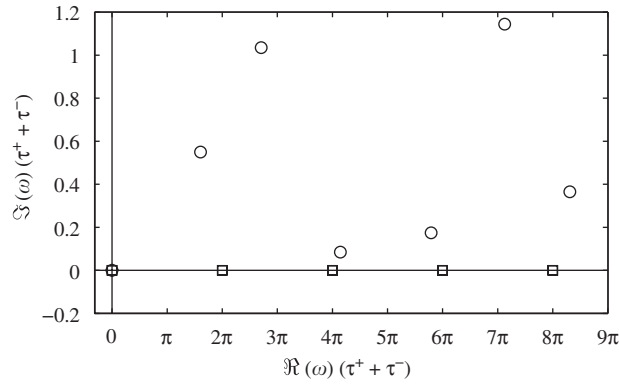
Fig. 6. Poles of the two-microphone identification scheme (Eq. (16), squares) and the Multi-Microphone-Method (Eq. (22) for $n = 3$, circles) with $(\tau_{1,1}^+ + \tau_{1,1}^-)/(\tau_{1,2}^+ + \tau_{1,2}^-) = \sqrt{2}$.
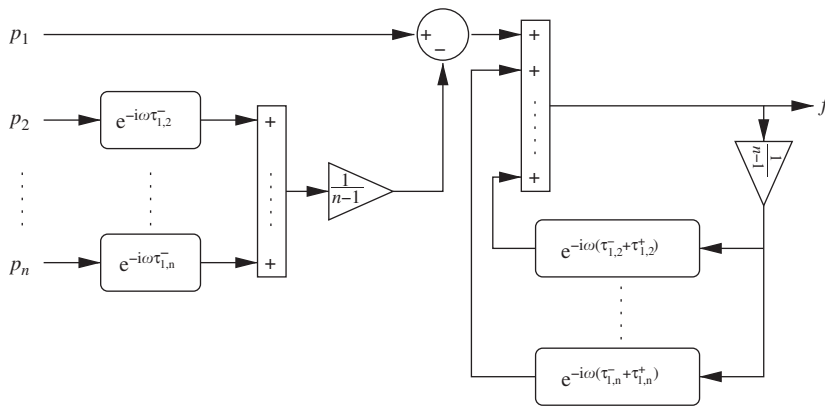

Fig. 7. Block diagram mapping n measured pressures to the downstream travelling wave f.

It is, however, more instructive to consider the frequency domain solution for $\hat{f}$, which is obtained from Eq. (21) as

$$\hat{f} = \frac{\hat{p}_1 - \dfrac{1}{n-1}\big(\hat{p}_2 e^{-i\omega\tau_{1,2}^-} + \cdots + \hat{p}_n e^{-i\omega\tau_{1,n}^-}\big)}{1 - \dfrac{1}{n-1}\big(e^{-i\omega(\tau_{1,2}^+ + \tau_{1,2}^-)} + \cdots + e^{-i\omega(\tau_{1,n}^+ + \tau_{1,n}^-)}\big)}. \tag{22}$$

The denominator in Eq. (22) has real zeros only where $\omega(\tau_{1,j}^+ + \tau_{1,j}^-) \bmod 2\pi = 0$ for all j. If the propagation delays associated with the microphone spacings are incommensurate, this will happen only at large frequencies (and at $\omega = 0$). Apart from this, all poles lie in the upper half of the ω-plane. A plot of the first few poles of Eqs. (16) and (22) for the case $n = 3$ is shown in Fig. 6.

Accordingly, a state-space realization of Eq. (22) is asymptotically stable and can be used to serve as the wave decomposer D, mapping n pressures to the downstream propagating wave, as shown in Fig. 2. The block diagram of the feedback scheme for this purpose is shown in Fig. 7.

Note, however, that when implementing Eq. (22) on a digital control board, Padé approximations for the time-delays should be used. Otherwise, rounding the time-delays to sample time will introduce inaccuracies, which might have a significant effect on the quality of the wave decomposition—even if the control board is run at several kilohertz. The Padé approximation of a time-delay is a finite dimensional approximation of $e^{-i\omega\tau}$ by a rational transfer function. The more microphones are used to determine the acoustic field, the more
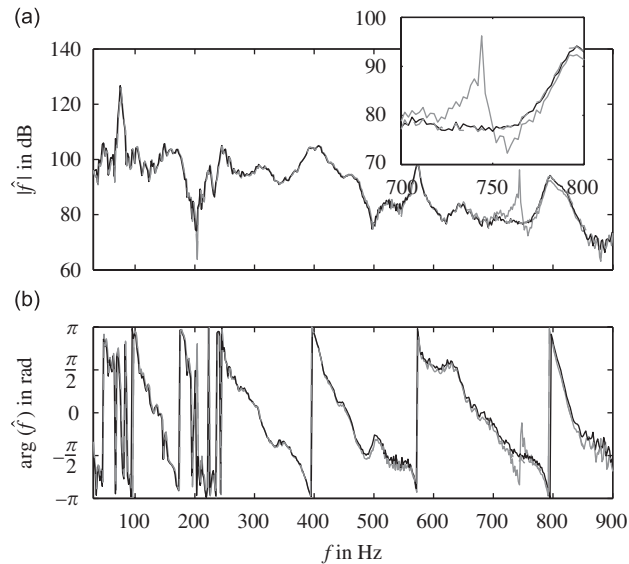
Fig. 8. Comparison of $\hat{f}$-wave (control input) calculated with MMM in frequency domain (black solid), MMM in time domain (grey dashed), TMM in time domain (grey solid): (a) magnitude and (b) phase between $\hat{f}$-wave and excitation signal of loudspeaker.

time-delays are involved and the larger is the state dimension of the controller. Using the online MMM instead of the TMM yields more accurate results on the one hand but requires more processor capacity on the other.

Fig. 8 compares the extracted f-waves obtained by three different identification schemes. As the f-wave is the control input, its identification has a huge impact on the accuracy of the adjusted closed-loop reflection coefficient. For the spectra shown, the test rig was operated at $\phi = 0.65$ and a thermal power of approx. 100 kW. Additionally, it was excited by a loudspeaker with a sweep signal ranging from 20 to 1000 Hz. The f-waves were calculated by cross-correlation with the excitation signal. In Fig. 8a, the magnitudes are compared proving that the f-wave identified with the MMM in time domain (grey dashed) is nearly identical to the one obtained from the traditional MMM in frequency domain (black solid). Results for the TMM in time domain (grey solid) are equally well, except for frequencies between 700 and 800 Hz. In this region, the restrictions of using the TMM close to frequencies given by Eq. (17) become obvious. At 744 Hz the microphone spacing is equal to half the wave-length. As can be seen in the enlarged frame, the error is not limited to this frequency but also affects neighbouring frequencies. Not only the magnitude but also the phase between the excitation signal and the generated f-wave has to be determined accurately. Results shown in Fig. 8b prove that the phases are in very good agreement, too. Note that if the impedance is to be tuned for cold flow conditions, the speed of sound and therefore the frequencies, at which Eq. (17) is satisfied, decrease.

4. Results of experiments

4.1. Experimental setup

Experiments were conducted in an atmospheric combustion test rig, which is schematically shown in Fig. 9. The combustor features a swirl-stabilized burner and is operated in lean-premixed mode. The diameter of the exhaust duct is 0.2 m and the burner has an area expansion ratio of approximately 4. A more detailed description of the burner can be found in Ref. [31]. To simulate conditions which are closer to those in full-scale engines, an electrical preheater can be used to provide higher air temperatures at the burner inlet. Several water-cooled microphones up- and downstream of the flame allow for full identification
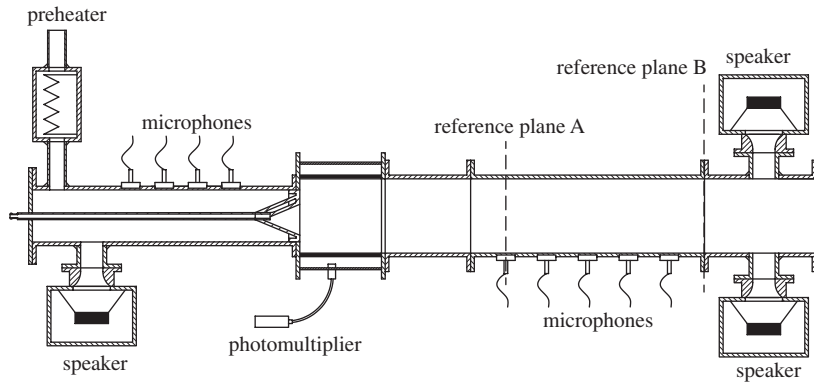
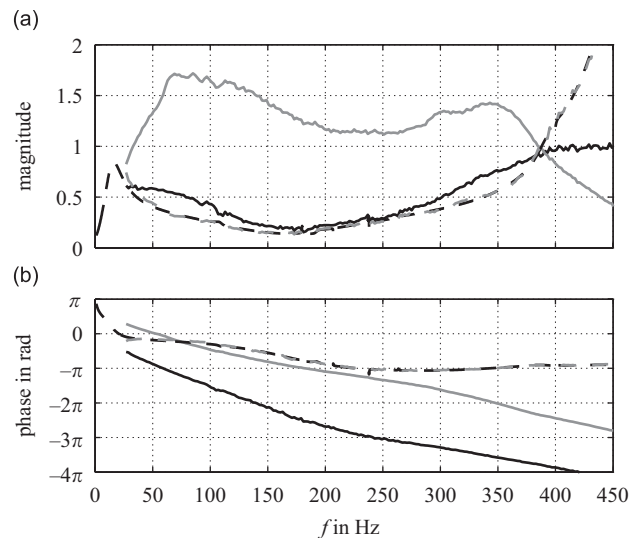Fig. 9. Schematic setup of the atmospheric test rig.

Fig. 10. Frequency responses for downstream reflection coefficient (black solid), loudspeaker (grey solid), and control law to adjust an anechoic end (grey dashed and black dashed): (a) magnitude and (b) phase.

of the plane wave pressure field. The OH-chemiluminescence in the flame is monitored with a photo-multiplier equipped with an optical bandpass filter that is connected to the combustion chamber via a fibre optic cable. In the zone where the flame stabilizes, a quartz glass tube allows for full optical access. Woofers, mounted at both ends of the rig, provide for acoustic excitation. The measurement tube where the downstream microphones are mounted and the section with the woofers have water-cooled walls. Additionally, the speaker casings are purged with air to prevent hot gases from entering. The combustor outlet can be equipped with different terminations, such as, e.g., an orifice to reduce the reflection of low-frequency acoustic waves [32,33].

The reference plane A drawn in Fig. 9 marks the location where the downstream travelling wave, serving as the control input, was identified. Plane B was taken as reference for the up- and downstream reflection coefficients and the speaker transfer function shown in the following sections. Note here that this plane is located upstream of the speaker casings. Therefore, the influence of the casings will be included in all reflection coefficients of the downstream end shown.

The controller ran on a DS1103 PPC control board (dSPACE), which generated the command signal for the woofers, at a sampling frequency of 2^{13} Hz.

To demonstrate how the reacting flow influences the controller's performance, due to the increased noise level, the impedance tuning concept was first applied to the cold flow for comparison.

4.2. Cold flow

In the case of cold flow, an air mass flow of 55 g/s was used. Fig. 10 shows the reflection coefficient (black solid) and the speaker transfer function (grey solid) for the case with the orifice plate mounted. The speaker transfer function sharply decreased at frequencies below 50 Hz and, though somewhat more moderate, above 350 Hz. According to Eq. (7), this resulted in a rapid increase of the controller transfer function in these frequency bands. This is generally not desirable because an increase of the controller transfer function leads to a strong amplification of the microphone signals and could, therefore, limit the actuator performance.

Additionally, the controller transfer function K to adjust a non-reflecting end, i.e., $R_{cl} = 0$, is plotted (Fig. 10, grey dashed). In this case, K was simply obtained as the ratio of the uncontrolled reflection coefficient and the speaker transfer function (see Eq. (7)). Unlike the measured K data, the identified controller model is valid for all frequencies between zero and infinity. Therefore, it has to be made sure that the model for the controller transfer function decreases for very low and high frequencies. This was achieved by adequately fitting the discrete frequency data as shown in Fig. 10. The identified model (dashed black curve) followed the measured speaker transfer function K down to approximately 30 Hz but for lower frequencies, where no measured values were available, it was forced to decrease. In the case shown, the identified model was of order 25.

Fig. 11 shows the uncontrolled downstream reflection coefficient (black solid) with the orifice plate mounted. It exhibited only slight reflection at frequencies below 300 Hz. Therefore, the pressure spectrum depicted in Fig. 12 shows no distinct resonance peaks. The test rig was excited with the upstream mounted loudspeaker, which was driven by a sweep, ranging from 30 to 500 Hz. At first, a non-reflecting end ($R_{cl} = 0$) was simulated. The solid grey curves in Figs. 11 and 12 show the results for this case. The magnitude of the reflection coefficient was reduced to values below 0.1 and in the range of 100 to 350 Hz even below 0.02, which is considerably lower than the reflection coefficient of technically realizable anechoic terminations. Here, the reflection coefficient generally lies between 0.1 and 0.2.

The acoustic impedance Z can take values ranging from 0 to infinity. Accordingly, the reflection coefficient R might take all values (see Eq. (3)) ranging from -1 (acoustically soft, pressure node) to $+1$ (acoustically
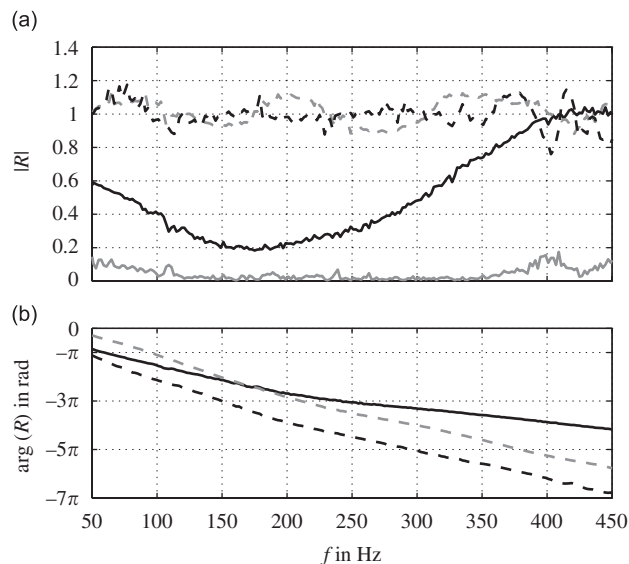

Fig. 11. Downstream reflection coefficient for the baseline case without control (black solid), $R_{cl} = 0$ (grey solid), $R_{cl} = +1$ with additional length $\Delta l = 0.5$ m (grey dashed), and $R_{cl} = -1$ with additional length $\Delta l = 0.5$ m (black dashed); non-reacting flow: (a) magnitude and (b) phase.
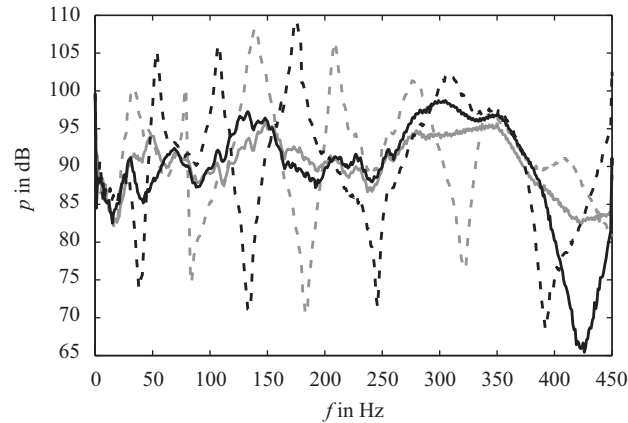
Fig. 12. Spectra of acoustic pressure for the baseline case without control (black solid), $R_{cl} = 0$ (grey solid), $R_{cl} = +1$ with additional length $\Delta l = 0.5$ m (grey dashed), and $R_{cl} = -1$ with additional length $\Delta l = 0.5$ m (black dashed); non-reacting flow.

Table 1
Resonance frequencies in Hz of a 2.5 m long duct with acoustically hard end upstream and acoustically hard ($R_{cl} = +1$), respectively, acoustically soft ($R_{cl} = -1$), boundary at its downstream end

n	$v = 0$, ($R_{cl} = +1$)		$p = 0$, ($R_{cl} = -1$)	
	Calc.	Exp.	Calc.	Exp.
1	69.2	78.5	39.4	54
2	138.4	138.5	103.8	107.5
3	207.6	209	173	175
4	276.8	276	242.2	–
5	346	347	311.4	308.5
6	415.2	410	380.6	–
7	484.4	484.5	449.8	452.5

hard, velocity node). If the impedance tuning concept is able to prescribe these extremal values and $R = 0$, it will be most probably able to adjust the whole range of possible reflection coefficients. Therefore, in a next step, the system was adjusted to totally reflecting as opposed to perfectly absorbing in the case of $R_{cl} = 0$. For convenience, the two cases are denoted as $R_{cl} = -1$ and $R_{cl} = +1$ in the following.

Fig. 11 proves that both cases could be realized with high accuracy (dashed grey and black curves, respectively). The magnitude of both reflection coefficients lay between 0.9 and 1.1 in the whole controlled frequency interval. The constant difference of π between the adjusted acoustically soft and acoustically hard end was clearly observable in the phase plot for all frequencies.

To show that the rig can be tuned to desired resonance frequencies, an additional length of 0.5 m was simulated. The actual test rig has an effective length of 2 m (including the end correction). Table 1 shows the calculated resonance frequencies of a 2.5 m long duct with an acoustically hard boundary at its upstream end and an acoustically soft, respectively, acoustically hard, boundary at its downstream end. These frequencies are compared to the resonances found in the experiments (see Fig. 12). If both boundaries of the duct are acoustically hard ($v = 0$), the resonance frequencies are given by

$$f = \frac{nc}{2l}. \tag{23}$$

If $p = 0$ at the downstream end, which is the case for an acoustically soft end,

$$f = \frac{(2n-1)c}{4l}. \tag{24}$$

Here, n is an integer ($n = 1, 2, \ldots$) and l is the duct length. The frequencies were calculated for a speed of sound of 346 m/s corresponding to the measured ambient temperature.

Comparison of the calculated resonance frequencies (Table 1) to the ones obtained through experiments (Fig. 12 and Table 1) underlines the feasibility of accurately prescribing resonances to a given test rig setup. Except for $n = 1$, the maximal deviation between calculation and experiments was approximately 1%. For an acoustically soft downstream end, two resonance frequencies, at 242.2 and 380.6 Hz, were not observed in the experiments. This was due to nodes in the axial pressure distribution.

4.3. Reacting flow

The test rig was operated in lean-premixed mode burning natural gas with an equivalence ratio of $\phi = 0.65$ at a thermal power of 110 kW. The flow entered the combustion chamber at ambient temperature. Two different end configurations of the downstream termination were used. One was an open (acoustically soft) end, thus, generating a pressure node at the downstream exit. In the other case, the test rig was equipped with an orifice. This configuration produced a relatively small magnitude of the reflection coefficient as acoustic energy was dissipated into vortices, shedding from the orifice's edge [32,33]. If not explicitly mentioned in the following, the controller was applied to the configuration with orifice and its transfer function (Eq. (7)) was identified for frequencies between 70 and 300 Hz.

In Fig. 13, the acoustic pressure spectra for the two configurations without control can be seen. For the case of the open end (black dashed), distinct peaks at 82 Hz and its multiples can be observed, representing the $\lambda/4$-mode of the rig. The effect of the orifice can clearly be seen (black solid). No strong pressure oscillations were existent anymore as it stabilized the combustion process by increasing the loss of acoustic energy across the downstream boundary. Mounting the orifice resulted in a peak amplitude reduction from 153 to 111 dB, i.e., a reduction to less than 1% of the pressure amplitude for the open end. The standing wave pattern disappeared, thus, indicating that mainly propagating acoustic waves were present, which is the case for a low-reflecting boundary. Fig. 14 depicts the reflection coefficients for these two configurations. For the open end (black dashed curve) the reflection coefficient was similar to the one described by the formula of Levine and Schwinger [34] for long wave-lengths. With the orifice mounted, $|R|$ was decreased to values around 0.3.

Using the impedance tuning concept, the reflection coefficient was changed to fully reflecting ($|R_{cl}| = 1$):

$$R_{cl} = +1 \cdot e^{i(\arg(R_{ol}) - \omega 2\Delta l/c)}. \tag{25}$$

Different virtual lengths could be simulated by adding an additional length Δl.

At first, the controller was used to generate an instability at 82 Hz corresponding to the frequency of the $\lambda/4$-mode of the open end. As can be seen in the phase plots of Fig. 14, the reflection coefficients' phases of both uncontrolled cases were nearly the same at the instability frequency. Therefore, the controller transfer
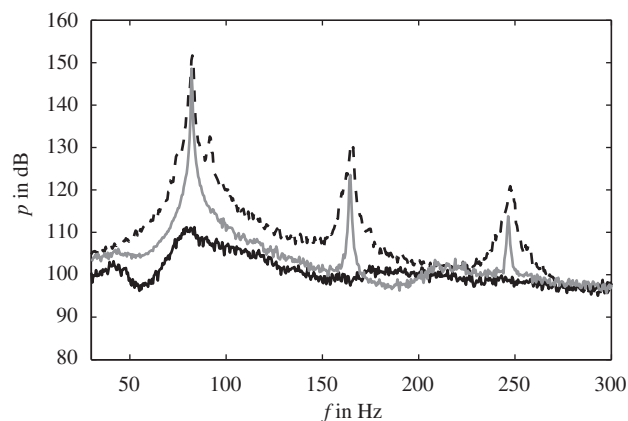

Fig. 13. Spectra of acoustic pressure for baseline case without control (with orifice, black solid—without orifice, black dashed) and $R_{cl} = +1$ with $\Delta l = 0$ m (grey solid); reacting flow.
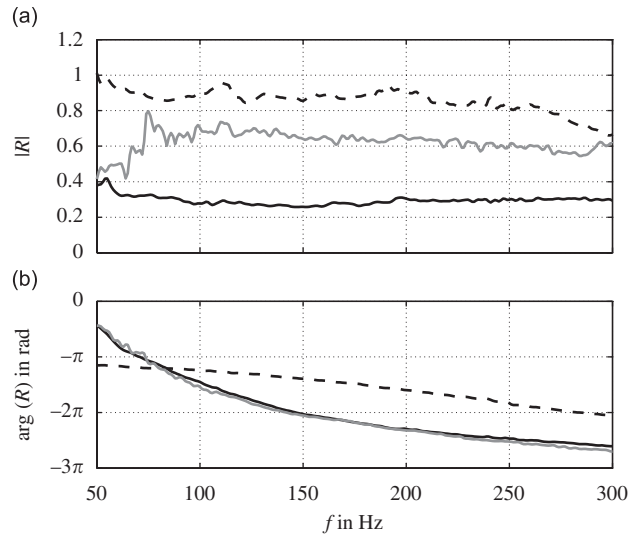
Fig. 14. Downstream reflection coefficient for the baseline case without control (with orifice, black solid—without orifice, black dashed) and $R_{cl} = +1$ with $\Delta l = 0$ m (grey solid); reacting flow: (a) magnitude and (b) phase.
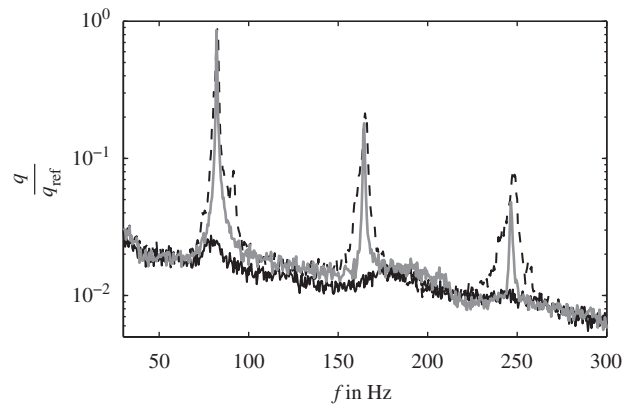

Fig. 15. Spectra of OH-chemiluminescence for baseline case without control (with orifice, black solid—without orifice, black dashed) and $R_{cl} = +1$ with $\Delta l = 0$ m (grey solid); reacting flow.

function was calculated to produce $|R_{cl}| = 1$ without changing the phase of the uncontrolled R_{ol} ($\Delta l = 0$ m). The solid grey curve shows the result for this case. Distinct peaks at 82 Hz and its multiples can be observed (grey solid in Fig. 13), proving that the anechoic end was virtually tuned to one with a higher reflection coefficient. Note that the test rig was not additionally excited by the upstream loudspeaker for all spectra shown. A peak amplitude of 150 dB was generated, 3 dB less than in the uncontrolled case without orifice.

Fig. 15 shows the impact of the generated acoustic field on the heat release fluctuation. Here, the scaled OH-chemiluminescence signals for the two uncontrolled cases (black dashed and solid) and the one for $|R_{cl}| = 1$ with $\Delta l = 0$ m (grey solid) are shown. A behaviour similar to the one of the pressure fluctuations in Fig. 13 can be observed. Large heat release fluctuations occurred at the instability frequency of 82 Hz (open end, black dashed), whereas no peaks are visible for the anechoic termination without control (black solid). In case of control (grey solid), the effect of the generated acoustic field on the heat release was the same as for the open end without control.

In Fig. 16, the phase portrait of the pressure fluctuation is depicted. The time-delay phase portrait is a convenient means to visualize the properties of dynamical systems. In the phase portrait shown here, the
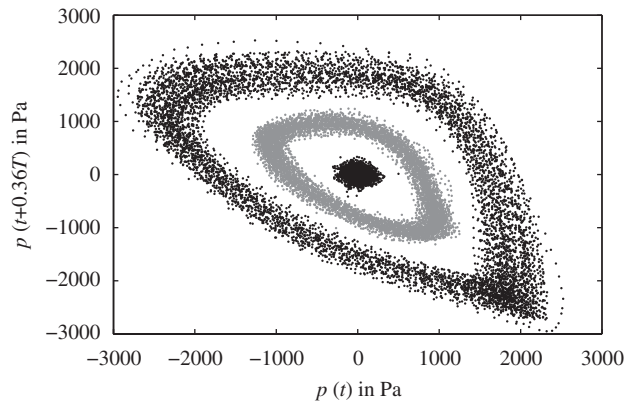
Fig. 16. Phase portrait of acoustic pressure for baseline case without control (with orifice, black (scattered around the origin)—without orifice, black orbit) and $R_{cl} = +1$ with $\Delta l = 0$ m (grey orbit); reacting flow.
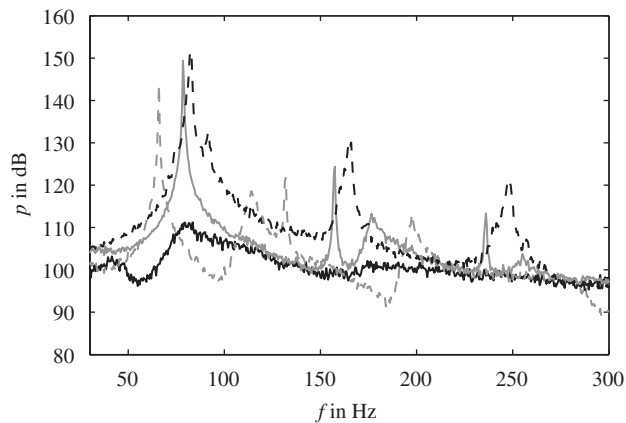

Fig. 17. Spectra of acoustic pressure for baseline case without control (with orifice, black solid—without orifice, black dashed), $R_{cl} = +1$ with $\Delta l = 0.5$ m (grey solid), and $R_{cl} = +1$ with $\Delta l = 2$ m (grey dashed); reacting flow.

unsteady acoustic pressures at time t and $t + \Delta t$ are plotted against each other. The time-delay Δt was set to $0.36\,T$, T being the period of the main instability frequency. The choice of Δt is somewhat arbitrary and orientated to the one chosen in Ref. [35]. Choosing a different time-delay would yield similar results. A system which oscillates at one single frequency (limit-cycle) has an elliptic orbit. If harmonics occur, this elliptic shape will be distorted. The appearance of noise causes the orbit to become fuzzy [36], i.e., the orbit changes more or less slightly from cycle to cycle. If the system is stable and only forced by noise, it will be concentrated about one point. Lieuwen [35] and Rowley et al. [36] investigated this visualization method in detail. For the uncontrolled case (open end), the phase portrait of the pressure showed the characteristic noisy limit-cycle (Fig. 16 black orbit). With the orifice mounted, the pressure fluctuations were scattered around the origin (black). In this case, the system was only driven by noise. For the controlled case, the system could be pushed to an orbit (grey), proving that it was in a limit-cycling state. However, this orbit was smaller than in the uncontrolled case without orifice. The difference between the orbit radii was larger than that of the peak amplitudes at 82 Hz (3 dB, i.e., a factor of $\sqrt{2}$, Fig. 13). This was due to the fact that in the uncontrolled case the system exhibited slight variations of the oscillation frequency. Generally, a combustion process is highly unsteady causing cycle-to-cycle variations and thus the oscillation frequency to be shifted around its main oscillation frequency. The peak in the spectrum was much broader, as can be seen in Fig. 13. Additionally, in case of no control, the orbit was more scattered as the overall noise level was higher.
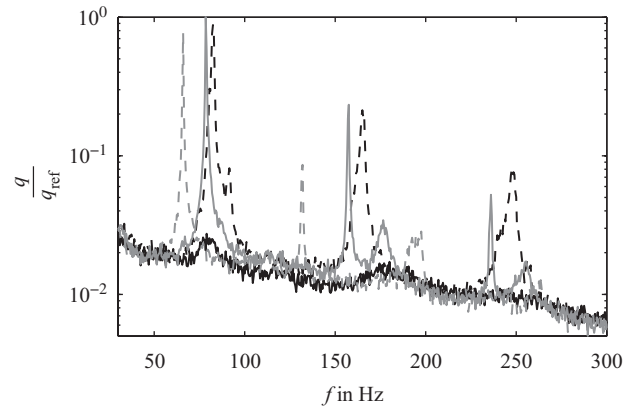
Fig. 18. Spectra of OH-chemiluminescence for baseline case without control (with orifice, black solid—without orifice, black dashed), $R_{cl} = +1$ with $\Delta l = 0.5$ m (grey solid), and $R_{cl} = +1$ with $\Delta l = 2$ m (grey dashed); reacting flow.
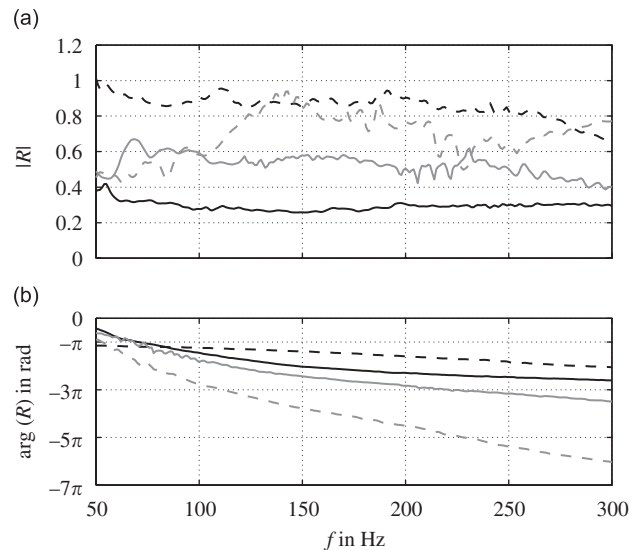

Fig. 19. Downstream reflection coefficient for the baseline case without control (with orifice, black solid—without orifice, black dashed), $R_{cl} = +1$ with $\Delta l = 0.5$ m (grey solid), and $R_{cl} = +1$ with $\Delta l = 2$ m (grey dashed); reacting flow: (a) magnitude and (b) phase.

Regarding the phases of the reflection coefficients (Fig. 14), it can be stated that they were equal for the case of control (solid grey) and the uncontrolled case (black solid), as prescribed. The magnitude of the measured reflection coefficient, however, was between 0.6 and 0.7, thus, differing from the desired value of $|R_{cl}| = 1$. This was due to the fact that the output calculated by the controller had to be restricted to 70% of the actual value, as otherwise the woofers' amplifiers went into saturation. Hence, the saturation was not system-inherent compared to the uncontrolled case without orifice, in which the nonlinear saturation could be attributed to the flame response. Here, the actuator power was the limiting factor.

In a next step, the test rig length was virtually extended by manipulation of the reflection coefficient's phase. Consequently, the instability peak was shifted to lower frequencies. The solid and the dashed grey curves in Fig. 17 shows the pressure spectra for additional lengths of $\Delta l = 0.5$ and 2 m, shifting the pressure peaks to 79 and 66 Hz, respectively. The same holds for the heat release fluctuations depicted in Fig. 18. Virtually extending the test rig length resulted in a larger slope of the reflection coefficient's phase as the propagation time of, and thus the time-delay between, the incident and the reflected wave became larger (solid and dashed grey curves in Fig. 19). If the phase decrease $\partial \varphi / \partial f$ is merely associated with a time-delay, the adjusted
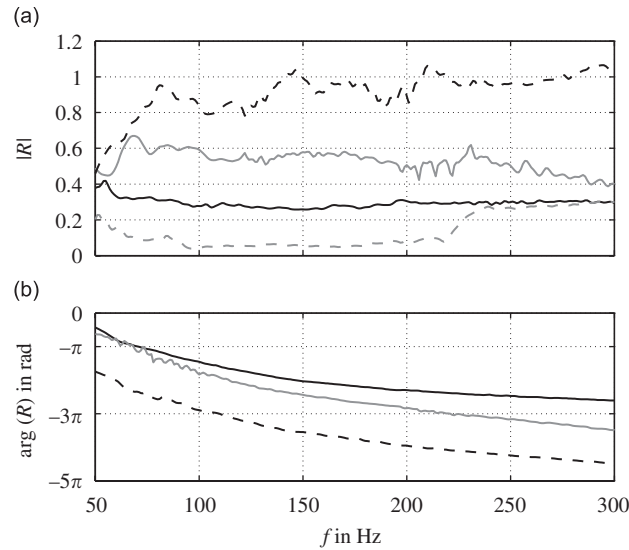
Fig. 20. Downstream reflection coefficient for the baseline case without control (with orifice, black solid), $R_{cl} = +1$ with $\Delta l = 0.5$ m (grey solid), $R_{cl} = -1$ with $\Delta l = 0.5$ m (black dashed), and $R_{cl} = 0$ (grey dashed); reacting flow: (a) magnitude and (b) phase.

additional length Δl can easily be calculated from the measured reflection coefficient's phase. Using

$$\Delta l = -\frac{1}{4\pi c}\frac{\Delta(\varphi_{cl} - \varphi_{ol})}{\Delta f} \tag{26}$$

yields this length, because the difference of φ_{cl} and φ_{ol} was only due to the prescribed additional length. For both virtual extensions, the difference in slopes matched perfectly the prescribed difference in lengths.

Apparently, imposing a fully reflecting boundary, resulted in an unstable system. By manipulating the phase of the downstream reflection coefficient, the frequency of oscillation could be adjusted. Regarding the magnitudes of the downstream reflection coefficient for the controlled cases (grey curves in Figs. 14 and 19), it must be noted that they all differ from the adjusted value of $|R_{cl}| = 1$ due to limited actuator power. However, as can be seen in the spectra of all controlled cases (Figs. 13 and 17), the peaks were generated at the desired frequencies nonetheless. If actuators with sufficient acoustic power were available, the desired impedances could exactly be imposed, even for the case of an unstable system with high oscillation amplitudes.

In contrast to the previously imposed reflection coefficient of $R_{cl} = +1 \cdot \exp(i\,\arg(R_{ol}) - i\omega 2\Delta l/c)$, the controller was then used to generate $R_{cl} = -1 \cdot \exp(i\,\arg(R_{ol}) - i\omega 2\Delta l/c)$ with different lengths Δl. Note that unlike the results shown in the cold flow section, here, $R_{cl} = \pm 1$ cannot be referred to as acoustically hard and acoustically soft, as the phase of the uncontrolled R_{ol} was considered, too. Figs. 20 and 21 depict results for these cases. The reference configuration with orifice and without control is again plotted in black solid. For $R_{cl} = -1$ (black dashed) and $R_{cl} = +1$ (grey solid), Δl was set to 0.5 m. Here and in the following, the phase of R_{ol} (see Eq. (25)) is not explicitly indicated but has to be considered nonetheless. Regarding the phase plots (Fig. 20), they both exhibited the characteristic larger slope of an extended duct. There was a constant difference of π between them, corresponding to the difference in signs. Note that in case of $R_{cl} = -1$, it was possible to adjust a controller gain of 1 without getting into loudspeaker saturation. Therefore, the magnitude of the actually imposed reflection coefficient for $R_{cl} = -1$ was close to 1, whereas for $R_{cl} = +1$ it lay around 0.6, as seen previously. Additionally, the reflection was decreased to $R_{cl} = 0$ (grey dashed). Here, the controller transfer function was only identified up to 220 Hz. In this frequency range, the magnitude of R was decreased to values around 5%, which was equally good compared to the cold flow case.

Pressure spectra for the cases described above are shown in Fig. 21. With R_{cl} set to -1 and $\Delta l = 0.5$ m, two peaks were generated at 55 and 110 Hz. For $R_{cl} = 0$ (grey dashed) the spectra of the uncontrolled and controlled case were almost the same, due to the fact that the orifice already produced a low-reflecting end.
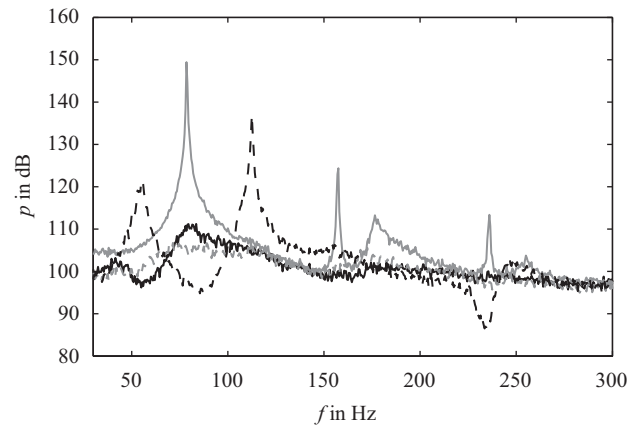
Fig. 21. Spectra of acoustic pressure for the baseline case without control (with orifice, black solid), $R_{cl} = +1$ with $\Delta l = 0.5$ m (grey solid), $R_{cl} = -1$ with $\Delta l = 0.5$ m (black dashed), and $R_{cl} = 0$ (grey dashed); reacting flow.
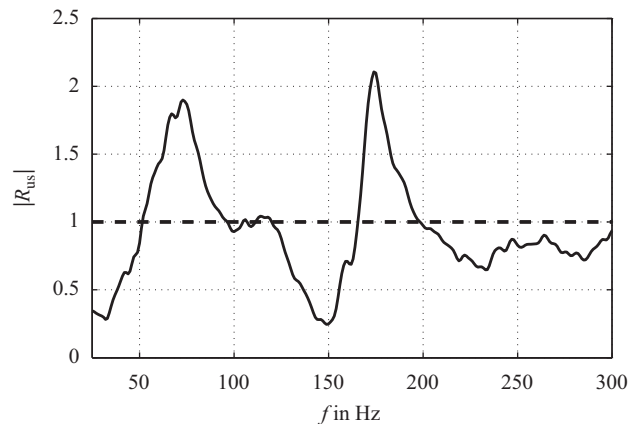

Fig. 22. Magnitude of the upstream reflection coefficient R_{us} for the uncontrolled case with the orifice plate mounted. The reflection coefficient comprised the flame response resulting in values larger than unity.

A question possibly arising when comparing the spectra of $R_{cl} = +1$ and $R_{cl} = -1$ in Fig. 21 with their corresponding downstream reflection coefficients in Fig. 20 is, why the pressure fluctuations for $R_{cl} = +1$ (grey solid) were six times higher (15 dB), although the magnitude of the downstream reflection coefficient was 25% smaller, i.e., more acoustic energy was lost through the downstream end. To understand this, consider the upstream reflection coefficient R_{us} shown in Fig. 22. It was measured by excitation with the downstream loudspeakers. To eliminate nonlinear effects resulting from high amplitude pressure oscillations caused by the thermoacoustic feedback cycle, it was measured with the orifice plate mounted at the downstream end. The reference plane (plane B in Fig. 9) lay downstream of the combustion zone and thus R_{us} comprised the flame response, the burner, and the fuel supply lines. In some frequency regions, it was larger than unity, showing the influence of the flame as an acoustically active element. These were the regions in which the system could get unstable if the phase relationship between the up- and the downstream reflection coefficient provided constructive interference and the magnitude of the downstream reflection coefficient was high enough. The shape of R_{us} explains why the peak for the case of $R_{cl} = +1$ was higher than the ones for $R_{cl} = -1$: At 82 Hz the acoustic wave amplification caused by the flame was considerably higher than at 55 and 110 Hz. Therefore, the flame produced more acoustic energy in this case. Note that the accuracy of the phase adjustment also has a governing influence on the amplitude of oscillation as for the thermoacoustic feedback cycle the phase relationship between R_{us} and R_{cl} is crucial. Thus, additionally to the difference in $|R_{us}|$, it might also be
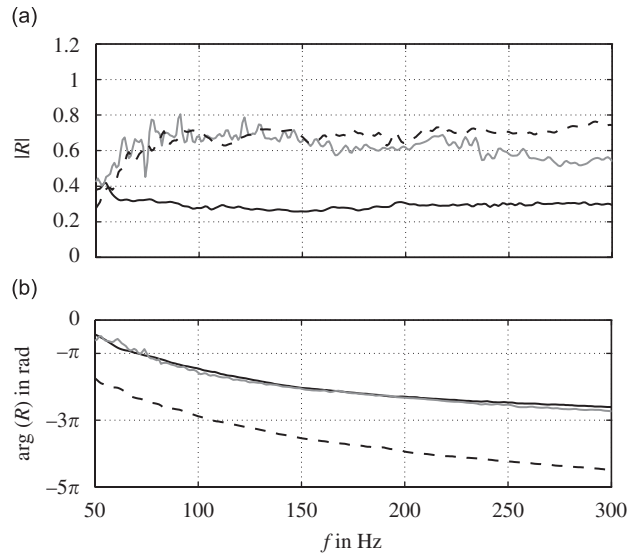
(a)

(b)

Fig. 23. Downstream reflection coefficient for the baseline case without control with orifice (black solid), $R_{cl} = +0.7$ with $\Delta l = 0$ m (grey solid), and $R_{cl} = -0.7$ with $\Delta l = 0.5$ m (black dashed); reacting flow: (a) magnitude and (b) phase.
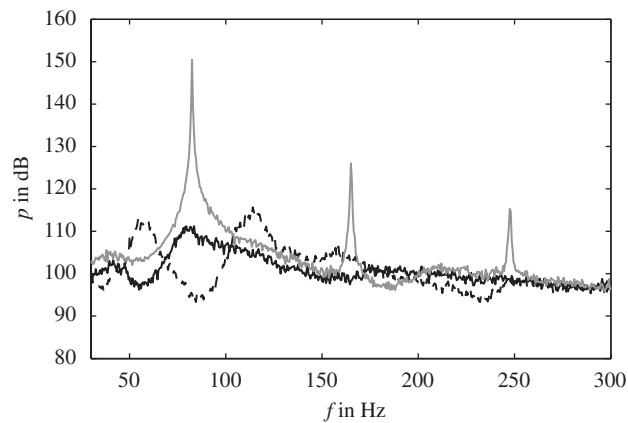

Fig. 24. Spectra of acoustic pressure for the baseline case without control with orifice (black solid), $R_{cl} = +0.7$ with $\Delta l = 0$ m (grey solid), and $R_{cl} = -0.7$ with $\Delta l = 0.5$ m (black dashed); reacting flow.

possible that the phase for $R_{cl} = +1$ was adjusted slightly more accurately than it was the case for $R_{cl} = -1$. More information on the phase adjustment can be found in Ref. [37].

Because in most previous settings the controller gain had to be limited to 70% of the prescribed value to prevent the loudspeaker control signals from saturation, R_{cl} was set to $\pm 0.7 \cdot \exp(i \arg(R_{ol}) - i\omega 2\Delta l/c)$. Through this, the full control gain could be used to prove that the magnitude of R could be adjusted properly if the loudspeaker signals were not saturated. As shown in Fig. 23, the magnitude of R was almost exactly set to 0.7 for both settings chosen: $R_{cl} = +0.7$, $\Delta l = 0$ m (grey solid) and $R_{cl} = -0.7$, $\Delta l = 0.5$ m (black dashed). Again, the phases differed by π and the different additional lengths.

For reasons of completeness, the pressure spectra are shown in Fig. 24. For $R_{cl} = +0.7$ (grey solid) strong oscillations were generated at 82 Hz, as was seen previously in Fig. 13. In contrast to $R_{cl} = -1$, no distinct peaks were generated as the magnitude was decreased to $R_{cl} = -0.7$ (black dashed).

Unlike all results shown previously, the scheme was also applied to a configuration in which relatively strong pressure pulsations were initially present. By doing so, another advantage of the control scheme becomes clear: it can also be used to suppress oscillations caused by thermoacoustic feedback. Reducing the
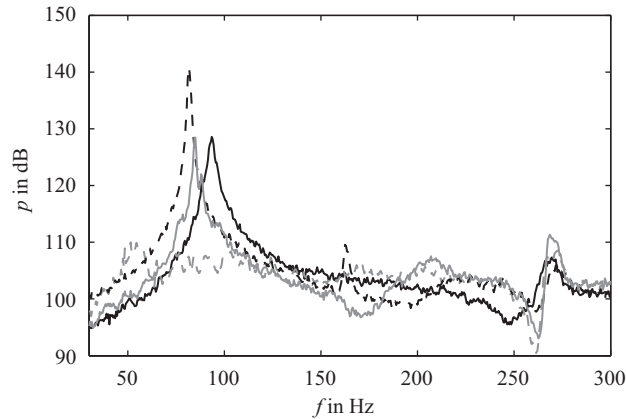
Fig. 25. Spectra of acoustic pressure for the baseline case without control (black solid), $R_{cl} = 0$ (grey dashed), $R_{cl} = +1$ with $\Delta l = 0.5$ m (black dashed), and $R_{cl} = R_{ol}$ with $\Delta l = 0.5$ m (grey solid); reacting flow.
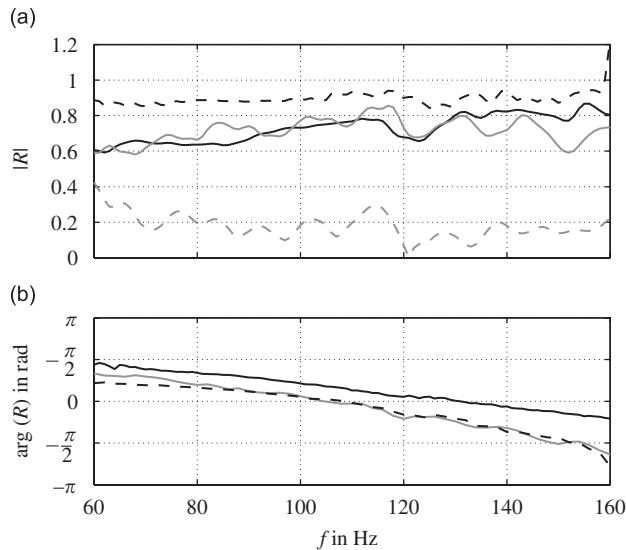

Fig. 26. Magnitude and phase of the downstream reflection coefficient for the baseline case without control (black solid), $R_{cl} = 0$ (grey dashed), $R_{cl} = +1$ with $\Delta l = 0.5$ m (black dashed), and $R_{cl} = R_{ol}$ with $\Delta l = 0.5$ m (grey solid); reacting flow: (a) magnitude and (b) phase.

downstream reflection coefficient corresponds to increasing the acoustic energy loss across the system boundaries. If the energy loss exceeds the net energy gain through the feedback mechanism, this results in a stable system (see, e.g., Ref. [38]). Bothien et al. [25] and Bloxsidge et al. [39] used this fact to suppress thermoacoustic instabilities in premixed combustors. Fig. 25 depicts the results for this case. Without control (black solid), a peak is observed at 94 Hz, somewhat higher than in the operating conditions discussed above, because here, the air was preheated to 423 K and ϕ was set to 0.7. The grey dashed curve represents the results for $R_{cl} = 0$. The controller was able to attenuate the peak by more than 20 dB.

Additionally, R_{cl} was adjusted to $R_{cl} = +1 \cdot \exp(\mathrm{i}\,\arg(R_{ol}) - \mathrm{i}\omega 2\Delta l/c)$ (black dashed) and $R_{cl} = |R_{ol}| \cdot \exp(\mathrm{i}\,\arg(R_{ol}) - \mathrm{i}\omega 2\Delta l/c)$ (grey solid), both with $\Delta l = 0.5$ m. Both prescribed conditions were successfully achieved as the pressure peaks were shifted to lower frequencies, according to the additional virtual lengths. For $R_{cl} = +1$, the system oscillated at 82 Hz and for $R_{cl} = R_{ol}$ with a changed phase, the peak was shifted to 85 Hz. As only the phase of the downstream reflection coefficient was changed, the amplitude of the pressure pulsation remained the same. The results prove that, as well as in the case with anechoic termination, the

impedance tuning concept was able to impose the desired boundary conditions in presence of pressure oscillations in the uncontrolled case. However, the frequency band in which a controller could be identified was smaller than in the previously shown cases. The downstream reflection coefficient was only adjusted between 60 and 160 Hz (instead of 70–300 Hz). The corresponding reflection coefficients are shown in Fig. 26.

5. Conclusions and outlook

It was shown how a feedback control scheme can be used to change the acoustic boundary condition of a combustion test rig. Multiple pressure measurements were used to decompose the acoustic field online to create the control input. The signal was processed by a suitable control law and fed back via an acoustic actuator mounted to the lateral boundary. The actuator manipulated the acoustic field in the system according to the prescribed boundary condition.

The impedance tuning approach was applied to a swirl-stabilized lean-premixed combustor. Both reacting and non-reacting flow conditions were investigated. The reflection coefficient was adjusted to fully reflecting (acoustically hard and acoustically soft). Note that the turbine inlet of a gas turbine normally represents a choked boundary condition corresponding to an acoustically hard termination. Therefore, the control scheme allows imposing the acoustics of a choked flow to an atmospheric test rig, where the flow is not choked. Furthermore, a non-reflecting termination was realized resulting in a reflection coefficient of 0.05 in a frequency band of several hundred Hertz. In addition to that, a virtual additional length was imposed to simulate different acoustic resonance frequencies at the same test rig. The concept proved to be of high accuracy in tuning the test rig to the desired resonance frequencies. This can be a crucial step in the burner design process since combustion test rigs usually do not exhibit the same acoustic behaviour as the full-scale engines. By applying the impedance tuning concept, the engine behaviour of new burners can be determined in the early design phase prior to testing them in the full-scale engine. Through this, the development process of new burner generations would become much more time- and cost-efficient.

A further application of the proposed approach is the active control of combustion instabilities. Since the reflection of acoustic waves at the combustor outlet is a crucial component for the thermoacoustic feedback loop, imposing an absorbing boundary condition has a highly stabilizing effect.

The availability of suitable actuators poses the fundamental problem for application of the impedance tuning concept to pressurized industrial test rigs with higher thermal power. The main requirements of such actuators are the acoustic power output and the delay times between command signal and actuator output, which have to meet the demands of the feedback control scheme. Another problem is the need for a proportional response over a relatively large bandwidth. Loudspeakers are not able to introduce enough acoustic power to these systems to cause a change of the system boundaries. Moreover, they would not withstand the harsh environmental conditions. Therefore, developing appropriate actuators is one of the most important tasks and a main issue of ongoing research.

References

[1] T.C. Lieuwen, V. Yang (Eds.), *Combustion Instabilities in Gas Turbine Engines, Progress in Astronautics and Aeronautics*, vol. 210, AIAA, Inc., New York, 2005.
[2] S. Rea, S. James, C. Goy, M.J.F. Colechin, On-line combustion monitoring on dry low NO_x industrial gas turbines, *Measurement Science and Technology* 14 (7) (2003) 1123–1130.

[3] H. Mongia, T. Held, G. Hsiao, R. Pandalai, Challenges and progress in controlling dynamics in gas turbine combustors, *Journal of Propulsion and Power* 19 (5) (2003) 822–829.

[4] H. Streb, B. Prade, T. Hahner, S. Hoffmann, Advanced burner development for the VX4.3A gas turbines, ASME Paper 2001-GT-0077, 2001.

[5] J.R. Seume, N. Vortmeyer, W. Krause, J. Hermann, C.-C. Hantschk, P. Zangl, S. Gleis, D. Vortmeyer, A. Orthmann, Application of active combustion instability control to a heavy duty gas turbine, *Journal of Engineering for Gas Turbines and Power* 120 (1998) 721–726.

[6] G.A. Richards, J.D. Thornton, E.H. Robey, L. Arellano, Open-loop active control of combustion dynamics on a gas turbine engine, *Journal of Engineering for Gas Turbines and Power* 129 (1) (2007) 38–48.

[7] V. Bellucci, P. Flohr, C.O. Paschereit, F. Magni, On the use of Helmholtz resonators for damping acoustic pulsations in industrial gas turbines, *Journal of Engineering for Gas Turbines and Power* 126 (2) (2004) 271–275.

[8] P. Berenbrink, S. Hoffmann, Suppression of dynamic combustion instabilities by passive and active means, ASME Paper 2000-GT-0079, 2000.

[9] G.A. Richards, D.L. Straub, E.H. Robey, Passive control of combustion dynamics in stationary gas turbines, *Journal of Propulsion and Power* 19 (5) (2003) 795–810.

[10] C.M. Jones, J.G. Lee, D.A. Santavicca, Closed-loop active control of combustion instabilities using subharmonic secondary fuel injection, *Journal of Propulsion and Power* 15 (4) (1999) 584–590.

[11] T.J. Poinsot, A.C. Trouve, D.P. Veynante, S.M. Candel, E.J. Esposito, Vortex-driven acoustically coupled combustion instabilities, *Journal of Fluid Mechanics* 177 (1987) 265–292.

[12] T. Lieuwen, Y. Neumeier, Nonlinear pressure-heat release transfer function measurements in a premixed combustor, *Proceedings of the Combustion Institute*, vol. 29, 2002, pp. 99–105.

[13] D. Guicking, K. Karcher, Active impedance control for one-dimensional sound, *Journal of Vibration, Acoustics, Stress, and Reliability in Design* 106 (1984) 393–396.

[14] M. Furstoss, D. Thenail, M.A. Galland, Surface impedance control for sound absorption: direct and hybrid passive/active strategies, *Journal of Sound and Vibration* 203 (2) (1997) 219–236.

[15] J.P. Smith, B.D. Johnson, R.A. Burdisso, A broadband passive-active sound absorption system, *Journal of the Acoustical Society of America* 106 (5) (1999) 2646–2652.

[16] Y. Li, G.-C. Chiu, L. Mongeau, Dual-driver standing wave tube: acoustic impedance matching with robust repetitive control, *IEEE Transactions on Control Systems Technology* 12 (6) (2004) 869–880.

[17] B. Schuermans, V. Bellucci, C.O. Paschereit, Thermoacoustic modeling and control of multi burner combustion systems, ASME Paper 2003-GT-38688, 2003.

[18] M.R. Bothien, J.P. Moeck, A. Lacarelle, C.O. Paschereit, Time domain modelling and stability analysis of complex thermoacoustic systems, *Proceedings of the Institution of Mechanical Engineers, Part A: Journal of Power and Energy* 221 (5) (2007) 657–668.

[19] W. Krebs, P. Flohr, B. Prade, S. Hoffmann, Thermoacoustic stability chart for high-intensity gas turbine combustion systems, *Combustion Science and Technology* 174 (7) (2002) 99–128.

[20] J. Kopitz, A. Huber, T. Sattelmayer, W. Polifke, Thermoacoustic stability analysis of an annular combustion chamber with acoustic low order modeling and validation against experiment, ASME Paper GT2005-68797, 2005.

[21] S. Evesque, W. Polifke, Low-order acoustic modelling for annular combustors: validation and inclusion of modal coupling, ASME Paper GT-2002-30064, 2002.

[22] V. Bellucci, B. Schuermans, D. Nowak, P. Flohr, C.O. Paschereit, Thermoacoustic modeling of a gas turbine combustor equipped with acoustic dampers, *Journal of Turbomachinery* 127 (2) (2005) 372–379.

[23] B. Schuermans, H. Luebcke, D. Bajusz, P. Flohr, Thermoacoustic analysis of gas turbine combustion systems using unsteady CFD, ASME Paper GT2005-68393, 2005.

[24] M. Zhu, A.P. Dowling, K.N.C. Bray, Transfer function calculations for aeroengine combustion oscillations, *Journal of Engineering for Gas Turbines and Power* 127 (1) (2005) 18–26.

[25] M.R. Bothien, J.P. Moeck, C.O. Paschereit, Experimental validation of linear stability analysis in premixed combustors supported by active control, *Proceedings of the 14th International Congress on Sound and Vibration*, 2007.

[26] C.O. Paschereit, B. Schuermans, W. Polifke, O. Mattson, Measurement of transfer matrices and source terms of premixed flames, *Journal of Engineering for Gas Turbines and Power* 124 (2) (2002) 239–247.

[27] T. Poinsot, C. le Chatelier, S.M. Candel, E. Esposito, Experimental determination of the reflection coefficient of a premixed flame in a duct, *Journal of Sound and Vibration* 107 (2) (1987) 265–278.

[28] M.L. Munjal, *Acoustics of Ducts and Mufflers*, Wiley, New York, 1987.

[29] B. Gustavsen, A. Semlyen, Rational approximation of frequency domain responses by vector fitting, *IEEE Transactions on Power Delivery* 14 (3) (1999) 1052–1061.

[30] M. Åbom, H. Bodén, Error analysis of two-microphone measurements in ducts with flow, *Journal of the Acoustical Society of America* 83 (6) (1988) 2429–2438.

[31] J.P. Moeck, M.R. Bothien, D. Guyot, C.O. Paschereit, Phase-shift control of combustion instability using (combined) secondary fuel injection and acoustic forcing, in: R. King (Ed.), *Active Flow Control, Notes on Numerical Fluid Mechanics and Multidisciplinary Design*, vol. 95, Springer, Berlin, 2007, pp. 408–421.

[32] D.W. Bechert, Sound absorption caused by vorticity shedding, demonstrated with a jet flow, *Journal of Sound and Vibration* 70 (3) (1980) 389–405.

[33] C.O. Paschereit, E. Gutmark, W. Weisenstein, Excitation of thermoacoustic instabilities by interaction of acoustics and unstable swirling flow, *AIAA Journal* 38 (6) (2000) 1025–1034.

[34] H. Levine, J. Schwinger, On the radiation of sound from an unflanged circular pipe, *Physical Review* 73 (4) (1948) 383–406.

[35] T.C. Lieuwen, Experimental investigation of limit-cycle oscillations in an unstable gas turbine combustor, *Journal of Propulsion and Power* 18 (1) (2002) 61–67.

[36] C.W. Rowley, D.R. Williams, T. Colonius, R.M. Murray, D.G. Macmynoski, Linear models for control of cavity flow oscillations, *Journal of Fluid Mechanics* 547 (2006) 317–330.

[37] M.R. Bothien, J.P. Moeck, C.O. Paschereit, Assessment of different actuator concepts for acoustic boundary control of a premixed combustor, ASME Paper GT2008-50171, 2008.

[38] A.P. Dowling, S. Hubbard, Instability in lean premixed combustors, *Proceedings of the Institution of Mechanical Engineers Part A: Journal of Power and Energy* 214 (4) (2000) 317–332.

[39] G.J. Bloxsidge, A.P. Dowling, N. Hooper, P.J. Langhorne, Active control of reheat buzz, *AIAA Journal* 26 (7) (1988) 783–790.